Chemistry–A European Journal
Research Article
doi.org/10.1002/chem.202300614
Chemistry Europe
European Chemical Societies Publishing
www.chemeurj.org

Can NbO Keep *nbo* Topology under Electrons? –Unveiling Novel Aspects of Niobium Monoxide at the Atomic Scale

Chengmin Li,[a, b, c] Junyan Li,[a, b, c, d] Yi Zhou,[a, b, c] Qing Zhang,[a, b, c] Alvaro Mayoral,*[e, f] Gang Li,*[a, g] and Osamu Terasaki*[a, b, c]

Abstract: A precise investigation of NbO has been carried out by advanced electron microscopy combined with powder and single crystal X-ray diffraction (XRD). The structure of pristine NbO has been determined as *Pm*-3 *m* space group (SG) with $a = 4.211$ Å and the positions of Nb and O at the 3*c* and 3*d* Wyckoff positions, respectively, which is consistent with previous report based on powder XRD data. Electron beams induced a structural transition, which was investigated and explained by combining electron diffraction and atomic-resolution imaging. The results revealed that the electron beam stimulated both Nb and O atom-migrations within each fcc sublattice, and that the final structure was SG *Fm*-3 *m* with $a = 4.29$ Å, Nb and O at the 4*a* and 4*b* with 75% occupancy and same chemical composition. Antiphase planar defects were discovered in the pristine NbO and related to the structural transformation. Theoretical calculations performed by density functional theory (DFT) supported the experimental conclusions.

Introduction

Transition metal oxides (TMO) have attracted a lot of interest because of their special physical and chemical properties.[1] Niobium belongs to the V-th family, Vanadium group, and has the electron configuration of $[Kr]4d^4 5s^1$ with various valences. It shows superconductivity below $T_c = 9.25$ K, and is widely used in industries for improving strength and toughness of steels.[2] Several niobium oxide phases, such as NbO, NbO_2, Nb_2O_5, and $Nb_{3n+1}O_{8n-2}$ ($n = 5$–8), have been reported.[3] Vanadium has the electron configuration of $[Ar]3d^3 4s^2$, has various valences, similar to Nb and therefore several oxide phases, VO, V_2O_3, V_nO_{2n-1} ($n = 3$–8), VO_2, V_nO_{2n+1} ($n = 3$, 4 & 6) and V_2O_5, have been also reported.[4] However, significant differences can be clearly observed between NbO and VO in their phase diagrams.[5] VO has a wide composition range similar to TiO. Both VO_x, ($0.8 \leq x \leq 1.3$) and TiO_y, ($0.7 \leq y \leq 1.25$) have the NaCl-type structure (space group, SG, *Fm*-3 *m*, #225) as a high-temperature phase with randomly distributed vacancies (point defects) in both metal and oxygen sublattices.[6] However, niobium monoxide shows a narrow phase existence of exactly 50% Nb and O compositions as a stoichiometric compound and it is stable in temperature and pressure up to 1920 K or 7.7 GPa, respectively, without phase transformation.[7]

Furthermore, NbO is of particular interest as it is the base example of the **nbo**-type net in reticular chemistry. This topology is proposed for a systematic enumeration and a series of metal–organic frameworks (MOFs) formed by different kinds of linkers were found sharing the same **nbo** net topology.[8] For a long time the structure of NbO was considered as a NaCl-type structure with 25% ordered vacancies in both the Nb and O sublattices. The topology, electronic states and bonding

[a] C. Li, J. Li, Y. Zhou, Q. Zhang, Prof. G. Li, Prof. O. Terasaki
School of Physical Science and Technology
ShanghaiTech University
Shanghai 201210 (China)
E-mail: alvaro.mayoral@unizar.es
ligang@shanghaitech.edu.cn
osamuterasaki@mac.com
[b] C. Li, J. Li, Y. Zhou, Q. Zhang, Prof. O. Terasaki
Centre for High-resolution Electron Microscopy (ChEM)
ShanghaiTech University
Shanghai 201210 (China)
[c] C. Li, J. Li, Y. Zhou, Q. Zhang, Prof. O. Terasaki
Shanghai Key Laboratory of High-resolution Electron Microscopy
ShanghaiTech University
Shanghai 201210 (China)
[d] J. Li
State Key Laboratory of Inorganic Synthesis and Preparative Chemistry
College of Chemistry
Jilin University
Changchun 130012 (China)
[e] Dr. A. Mayoral
Instituto de Nanociencia y Materiales de Aragón (INMA)
CSIC-Universidad de Zaragoza
Zaragoza 50009 (Spain)
[f] Dr. A. Mayoral
Laboratorio de Microscopias Avanzadas (LMA)
Universidad de Zaragoza
Zaragoza 50180 (Spain)
[g] Prof. G. Li
ShanghaiTech Laboratory for Topological Physics
ShangaiTech University
Shanghai 201210 (China)

Supporting information for this article is available on the WWW under https://doi.org/10.1002/chem.202300614

structure were studied by theoretical calculations.[9] Precise powder X-ray diffraction (PXRD) and neutron diffraction experiments suggested a cubic structure with the SG of *Pm*-3 *m* (#221) through extinction conditions from observed reflections, and then the structure model was proposed based on "ordered vacancies" without precise single crystal structure analysis. The model was the following: The Nb and O atoms are located at the 3*c* (face center) and 3*d* (edge) Wyckoff positions with site symmetry *m*-3 *m*, while vacancies occupy the sites of 1*a* (vertex) and 1*b* (body center) Wyckoff sites with site symmetry 4/*mmm*.[10]

If the occupation probabilities of Nb at the 3*c* and 1*a* sites and O at the 3*d* and 1*b* sites are different, then the extinction condition for *Pm*-3 *m*, would be fulfilled. Therefore, by diffraction alone it is insufficient to achieve a precise structure solution of NbO and the occupation probabilities still require a deeper investigation.

Additionally, the structure of NbO would be affected under different types of irradiation. A neutron radiation study of single crystal NbO revealed a structural transformation in which the atom occupancy increased in both the 1*a* and 1*b* sites for Nb and O, respectively, which returned into the original form at about 900 °C.[11] An electron microscopy (EM) study also showed a structural change under scanning transmission EM (STEM) revealing a significant variation at the vacancy columns.[12] These observations showed that the structure of NbO would change under different types of irradiations, but detailed information of this phenomenon is not clear yet.

In order to achieve a complete understating of the transformation that took place, EM offers several advantages unmatchable by other techniques. In STEM mode, the electron beam can be used as stimulation source for the structural transformation in a controlled way at the atomic level. By EM methods, both averaged and local structural information could be obtained by electron diffraction (ED) and high-resolution imaging.

In this work, we first measured both chemical composition and density followed by a structural study of the pristine NbO crystal by PXRD and single crystal X-ray diffraction (SCXRD) as precise as possible. This also gave a starting calibration for EM study on the pristine NbO crystal. We have used a multi-technique approach based on advanced electron microscopy methods, including C_s-corrected STEM imaging,[13] combined with ED approaches, selected area ED (SAED) and three-dimensional electron diffraction (3D ED).[14] Using C_s-corrected STEM, the structural transition process was observed from three electron-beam incidences along [100], [111], and [110] under a controlled electron dose.

At last, the structure solution of both, the pristine and the electron-beam-induced transformed Niobium monoxide, was obtained by electron crystallography combining SAED and 3D ED. Besides, an antiphase planar defect in the pristine NbO was observed, potentially related to the structural transformation. DFT calculations and Electron Energy Loss Spectroscopy (EELS) were performed together with the ED method to analyze and explain the electronic state and the structural transformation mechanism. A feature of duality with ionic and metallic properties was also revealed.

Results and Discussion

Initially, a precise analysis of the pristine NbO was performed through PXRD, SCXRD, elemental analysis, and density measurements to obtain the structure of the pristine material. To obtain a precise lattice parameter, PXRD was performed with Cu $K\alpha_1$ radiation in transmission mode, see Figure S1 and Table S1. the pristine NbO was identified as *Pm*-3 *m* SG with unit cell parameter $a = b = c =$ 4.211 Å. After measuring the density of NbO, 7.28 ± 0.01 g/cm^3, and the elemental composition Nb:O = 1:1 by Energy Dispersive X-ray Spectroscopy (EDS) and Electron Energy Loss Spectroscopy (EELS) elemental analysis (Figures S2–S4, Table S2), the unit cell was deduced as Nb_3O_3 (containing 3 Nb and 3 O per unit cell). Subsequently, SCXRD data was employed to solve the structure, 1745 reflections of a 95.1% completeness within 0.37 Å resolution were collected obtaining a pristine Nb_3O_3 structure with the unit cell $a = b = c$ = 4.2158 Å, $\alpha = \beta = \gamma = 90°$ and the *Pm*-3 *m* SG. The structure solution had a residual parameter R_1 = 3.85%. Figure 1 shows the structure solution of the pristine Nb_3O_3 solved by SCXRD, which is in agreement with the elemental analysis and the density measurement result. There are two Wyckoff sites with atoms at; 3*c* (0,1/2,1/2), (1/2, 0,1/2), (1/2, 1/2, 0) for Nb and 3*d* (1/2,0,0), (0,1/2,0), (0,0,1/2) for O.

In previous reports, Nb_3O_3 was described as 25% ordered vacancy with NaCl-type structure. In this description, vacancies are located at 1*a* (0,0,0) and 1*b* (1/2, 1/2, 1/2) sites, thus the 1*a* + 3*c* and 1*b* + 3*d* sites would form the Nb and O fcc sublattices, respectively. However, considering the definition of vacancy, which is a type of point defect in a crystal where an atom is missing from one of the lattice sites,[15] the occupation probability at vacancy positions may not be exactly 0%. Thus, the occupation probability at 1*a* and 1*b* in the pristine Nb_3O_3 structure, which was affected by the electron beam irradiation without breaking the symmetry of the *Pm*-3 *m* space group, requires further investigation. After obtaining the structure

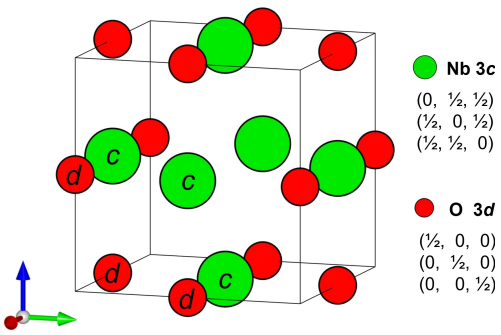

Figure 1. Structural model of pristine Nb_3O_3 solved by SCXRD. Green circles correspond to Nb and red ones to O. Wyckoff sites (*Pm*-3 *m*) are also indicated. The unit cell axes *a*, *b* and *c* are marked by red, green, and blue arrows, respectively.

solution of pristine Nb_3O_3, structure refinement considered various occupancies of the *a, b, c* and *d* sites using both SCXRD and PXRD data. See Figures S5-S6 and Tables S3-S8. The results revealed the precise solution for Nb_3O_3 with 100% occupancy at the 3*c* and 3*d* sites for Nb and O, respectively, and 0% occupancy at the 1*a* and 1*b* sites. The electron density map, Figure S7, reconstructed from the SCXRD data, also proved that no obvious residual electron density was found at the 1*a* and 1*b* positions, indicating that in the pristine Nb_3O_3 structure, the positions at 1*a* and 1*b* were not occupied by any atom.

Under EM observation when the sample was irradiated by the electron beam, we observed a structural transition. Figure 2 shows the structural evolution of Nb_3O_3 under electron beam irradiation. The C_s-corrected STEM-HAADF images of the first scan (pristine material), of the partially transformed and of the fully transformed structure which were extracted after continuous beam irradiation in scanning mode along the [100], [111] and [110] zone axes are depicted. For every micrograph the FFT diffractogram, plane group averaged image and the intensity line profiles are shown inset (all raw image frames, plane group averaged images and intensity profiles are shown in Figures S8-S10). Along the [100] direction (Figures 2a–c), five STEM frames were collected with the same electron dose, every image frame was recorded with a 0.04 × 0.04 Å^2 pixel size during 10 µs per pixel. Thus, the electron dose and total exposure time for each frame were 1.20 × 10^6 e/Å^2 and 10s. In the first frame (Figure 2a), the two signals were observed, attributed to the Nb (*c*) + O (*d*) columns and the Nb (*c*) + O vacancy (*b*) columns. In this mode, the columns containing the Nb vacancy (*a*) and O (*d*) were not visible. However, during irradiation of the materials, a faint signal began to appear in the Nb vacancy (*a*) + O (*d*) sites, suggesting that some Nb atoms in the *c* sites moved to the *a* sites or even replace O in the *d* sites.

Along the [111] direction (Figures 2d–f), eight STEM frames were collected continuously with 0.04 × 0.04 Å^2 pixel size during 5µs per pixel, the electron dose for this set was 5.99 ×

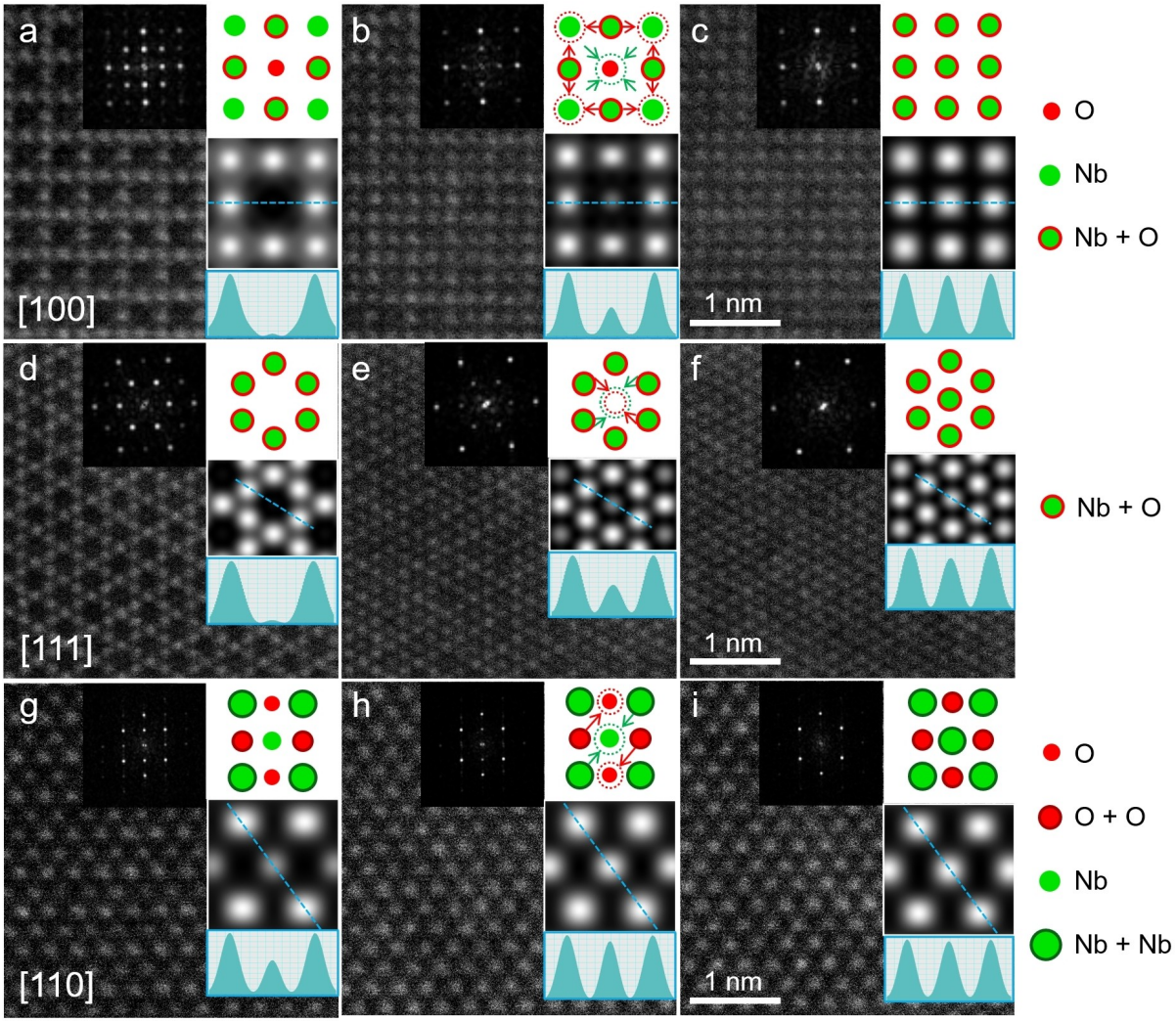

Figure 2. C_s-corrected STEM-HAADF images of Nb_3O_3 along [100] (a) Initial stage, (b) during transformation, (c) fully transformed. [111] (d) Initial stage, (e) partially transformed, and (f) fully transformed. [110] (g) Initial stage, (h) partially transformed, and (i) fully transformed. In every micrograph, FFT diffractograms, the plane averaged images (*p4 mm* along [100], *p6 mm* along [111], and *p2 mm* along [110]), the intensity profiles extracted from the dashed lines and the structural models viewed along corresponding directions are shown inset.

10^5 e/Å^2 and the total exposure time was 5 s. The first frame shows a Kagome lattice arrangement, formed by the signal from the Nb (*c*) + O (*d*) columns. The center of the hexagon corresponded to the columns with the Nb vacancy (*a*) + O vacancy (*b*), where, after irradiation, a signal emerged. It could be inferred that some of the Nb in the *c* sites moved to the *a* or *b* sites, but it could not be establish whether Nb in the *c* sites migrated to the *d* sites.

For [110] (Figures 2g–i), ten frames were collected with a 0.065 × 0.065 Å^2 pixel size during 5μs per pixel. Every frame was recorded with an electron dose of 2.27 × 10^5 e/Å^2 and a total exposure time of 5 s. The pristine structure (Figure 2g) shows two kinds of columns with different intensities, the Nb (*c*) + Nb vacancy (*a*), and the Nb (*c*) + Nb (*c*). As the STEM-HAADF contrast is sensitive to both atomic number and the amount of atoms in the columns, the intensity difference here corresponded to a different amount of atoms per column 1:2 respectively. During irradiation, the contrast difference of these two columns gradually decreased (Figure 2h) until the material fully transformed (Figure 2i), where all columns displayed similar intensity. This observation suggested that some Nb in the *c* sites moved to the Nb vacancy in the *a* site, and that the diffusion from *c* to the *b* (oxygen vacancy) or *d* sites (oxygen replacement) could be excluded since neither the pristine nor transformed STEM-HAADF images shows signals in columns where the O was present.

The total electron dose employed along the three orientations was decreased from 6 × 10^6 e/Å^2 along [100], to 4.8 × 10^6 e/Å^2 along [111] and finally 1.8 × 10^6 e/Å^2 along [110]; nevertheless, the transformation was completed within 50s. However, for a lower electron dose, the transformation was not observed.

This structural transition only took place in the region scanned by the electron probe. Figure S11 shows a low magnification C_s-corrected STEM-HAADF image from a NbO single crystal which was partially irradiated, where the atoms moved or re-arranged locally maintaining the crystallinity and the lattice. A transmission EM (TEM) image with the SAED patterns recorded from another partially irradiated NbO single crystal corroborate this behavior, see Figure S12. Elemental analysis performed by EELS collected from the pristine and from the fully transformed NbO proved that the elemental ratio was maintained being Nb:O = 1:1 (Figures S3–S4). Therefore, it is safe to assume that the chemical composition per unit cell was always Nb_3O_3 even during the transition.

The contrast of the atomic columns along the three main zone axes at different irradiation times was analyzed by measuring the intensity variation, shown in Figure S13. To clarify the relation between the SGs we introduced four parameters; V_a^{Nb}, V_c^{Nb}, V_b^{O} and V_d^{O}, which are vacancy concentrations in the Wyckoff positions *a, b, c* & *d* for *Pm*-3 *m*. Then, as the chemical composition per unit cell was maintained as Nb_3O_3 during the structural transition, the following apply: [I] For the Nb-sublattice, the 1*a* and 3*c* positions are occupied: V_a^{Nb} + Nb(1 - V_a^{Nb}) and 3{V_c^{Nb} + Nb(1- V_c^{Nb})}, respectively under the conditions, V_a^{Nb}+3 V_c^{Nb}=1.0 and $V_a^{Nb} \neq V_c^{Nb}$. [II] For the O-sublattice, the 1*b* and 3*d* positions are occupied: V_b^{O} + O(1 - V_b^{O}) and 3{V_d^{O} + O(1 - V_d^{O})}, respectively under the conditions, V_b^{O} + 3 V_d^{O} = 1.0 and $V_b^{O} \neq V_d^{O}$.

The atomic (column) arrangement, especially the Nb columns, (which gives the main Z-contrast in the STEM-HAADF images[16]), is significantly different along the [100] and [111] directions. Along the [110] such difference would not be so evident but should still be distinguishable as the amount of Nb atoms per column would change from 1:2 in the pristine material (*Pm*-3 *m*) to 1:1 in the transformed structure. Then, the theoretical intensity ratio in the STEM-HAADF images will be related to the ratio of Nb atoms. Along [100], two signals were measured, (*a* + *d* and *c* + *d*). The theoretical intensity ratio will be related to the ratio of Nb atoms: (1 - V_a^{Nb})/(1 - V_c^{Nb}). Along [111], the theoretical intensity ratio of the two measured columns (*a* + *b* and *c* + *d*) would be (1 - V_a^{Nb})/(1 - V_c^{Nb}). Along [110], the two measured columns (*a* + *c* and *c* + *c*) would display a theoretical intensity ratio of (2 - V_a^{Nb} - V_c^{Nb})/(2 - 2V_c^{Nb}). By measuring the intensity variation along the three main zone axes, (1 - V_a^{Nb})/(1 - V_c^{Nb}) would change from 0 to 1 along [100] and [111] direction. While, along [110] it would vary from 0.5 to 1 according to (2 - V_a^{Nb} - V_c^{Nb}) /(2 - 2V_c^{Nb}). As the amount of atoms per unit cell was constant; V_a^{Nb} + 3V_c^{Nb} = 1.0, it could be concluded that for the pristine material V_a^{Nb} = 1, V_c^{Nb} = 0, and at the final stage V_a^{Nb} = V_c^{Nb} = 0.25. This indicates that the electron-beam-induced structure transformation of Nb_3O_3 is from originally 0% and 100% occupancy for 1*a* and 3*c* sites respectively, to an equally 75% Nb occupancy.

ED analysis was also carried out to follow this transition. Initially, 3D ED was employed to collect the entire 3D reciprocal space of the structure before and after transformation to obtain the precise structure solution. Firstly, a 3D ED dataset and SAED patterns along the three main zone axes ([100], [111] and [110]) were collected minimizing the exposure to the electron beam. Secondly, the structural transformation of the same crystal was induced by an intense STEM probe, which was scanned along the crystal. After electron irradiation, the SAED patterns along the three main zone axes were collected. The complete structural transformation was corroborated when no additional changes were observed by either ED or imaging. At this stage, an additional 3D ED dataset was collected.

SAED patterns of the pristine crystal and of the fully transformed material are shown in Figure 3. For the pristine structure, the SAED patterns show a cubic P-lattice with no extinctions that appeared after irradiation. The reflections in the SAED patterns after irradiation could also be indexed by the same cubic lattice, but transformed from a P-lattice to an F-lattice. The reflection conditions are summarized as: 00 *l* (*l* = 2*n*), *hhl* (*h* + *l* = 2n), 0*kl* (*k, l* = 2*n*), *hkl* (*h* + *k, h* + *l, k* + *l* = 2*n*). Note that for some of the spots that gradually disappeared, it still remained a weak signal after transformation. However, after measuring the intensity of these reflections, they became lower by a factor of 10^2 than the remaining ones, indicating that the majority of the Nb_3O_3 structure had already transformed. The raw SAED patterns and line profile intensity measurements are shown in Figures S14–S16.

The two 3D ED datasets collected from the same crystal before and after transformation were used to reconstruct the

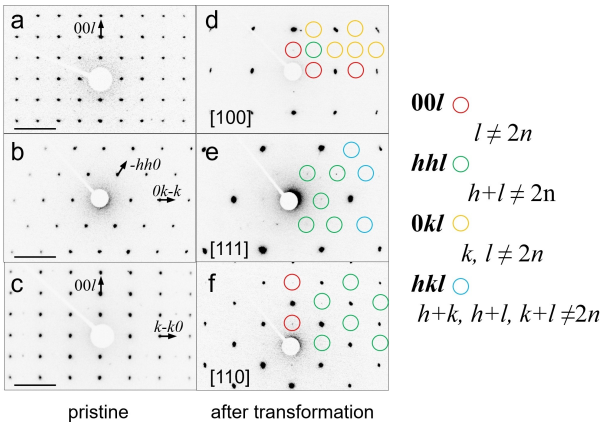

Figure 3. SAED patterns of NbO before (a, b, c) and after structure transformation (d, e, f) along [100], [111] and [110]. In the SAED patterns before transformation there were no extinctions, indicating a P-lattice. After electron irradiation, the SAED patterns show extinctions of 00 *l* (marked in red), *hhl* (green), 0*kl* (yellow) and *hkl* (blue). The scale bar corresponds to 5 nm^{-1}.

reciprocal space. The reflection intensities were then used to solve the two structures using the super flip method and later refined using *JANA 2020* software.[17] Figure S17 shows the slice-cut views of the reconstructed 3D reciprocal space along the three main zone axes as well as the solution models of these two structures. Table S9 shows the crystallographic information for the solved structures.

For the pristine Nb_3O_3, no extinctions were observed in the collected 3D ED data resulting in a structure solution within *Pm*-3 *m* SG. The final refined unit cell parameters were $a=b=c=4.21$ Å, $\alpha=\beta=\gamma=90°$. Figure S17d shows the pristine Nb_3O_3 model. The reciprocal intensity completeness was 99.0% in 0.4 Å resolution, and the residual parameter R_1 of this structure solution was 21.27%. The structure solution, Nb and O locating at 3*c* sites and 3*d* sites, respectively, in agreement with the reported and calculated data (density, elemental composition and SCXRD), where every unit cell contains 3(Nb + O) atoms.

The same process was applied after transformation. In this dataset, the electron diffraction shows significant extinctions (see Figures S17e-g). The diffraction conditions were 00 *l* ($l=2n$), *hhl* ($h+l=2n$), 0*kl* (*k*, $l=2n$), *hkl* ($h+k$, $h+l$, $k+l=2n$). These diffraction conditions corresponded to an F-lattice in agreement with the SAED observations. The structure solution was obtained with the SG of *Fm*-3 *m*. Figure S17h shows the model after structure solution and refinement with a slightly expanded unit cell $a=b=c=4.29$ Å, $\alpha=\beta=\gamma=90°$. This structure solution had a residual parameter $R_1=10.92\%$ and the data completeness was 100% with 0.5 Å resolution.

By combining the information obtained from the SAED patterns, the 3D ED structures determined before and after electron irradiation, and the sequential C_s-corrected STEM-HAADF images, it can be deduced that the structural transformation occurs from Nb_3O_3 (*Pm*-3 *m*) with Nb and O at the 3*c* and 3*d* sites ($V_a^{Nb} = V_b^{O} = 1$; $V_c^{Nb} = V_d^{O} = 0$), to a transition state, in which V_a^{Nb} and V_b^{O} were larger than 0.25 while maintaining the *Pm*-3 *m* SG, and to a final stage in which both V_a^{Nb} and V_b^{O} reached to 0.25, with 75% occupancy of Nb at 1*a* and 3*c*, and 75% occupancy of O at 1*b* and 3*d*. The SG of final stage was then transformed into *Fm*-3 *m*, and Nb and O would locate at 4*a* and 4*b* sites (4*a* in *Fm*-3 *m* comes from equalized 1*a* and 3*c* sites in *Pm*-3 *m* and 4*b* in *Fm*-3 *m* comes from equalized 1*b* and 3*d* sites). Schematic models of the pristine, transition state and fully transformed structures are shown in Figure 4.

To further identify the atom migration, especially to confirm the composition maintenance of Nb_3O_3 per unit cell rather than Nb_4O_4 of ideally rock salt structure, DFT calculations were employed to investigate the transformation mechanism. Figure 5a shows the calculated Electron Energy Loss Function (EELF) based on the pristine *Pm*-3 *m* Nb_3O_3 and on the *Fm*-3 *m* rock salt structure with 100% occupancy of the 4*a* and 4*b* sites (denoted by Nb_4O_4) and the experimental EELS data collected from the same area before and after transformation. The

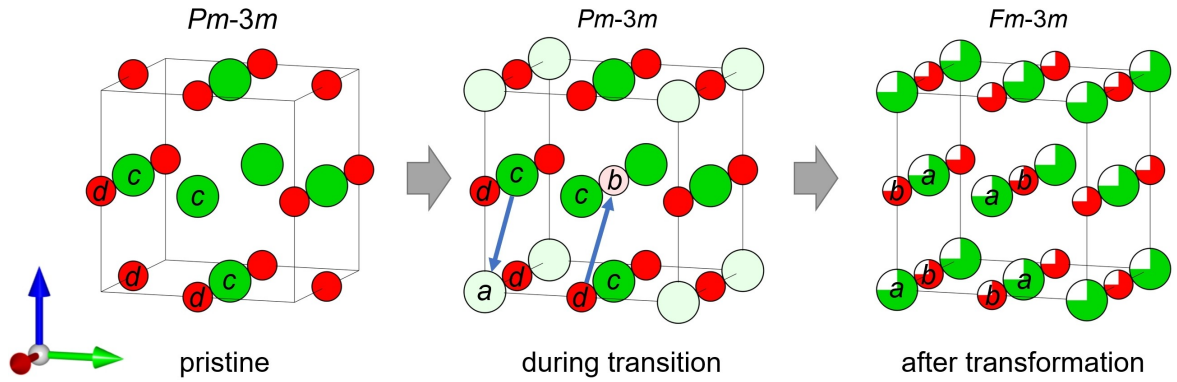

Figure 4. Illustration of the electron-beam-induced structural transition of Nb_3O_3 in the pristine stage, during the transition, and after the transformation. In the pristine stage, Nb and O locate at the 3*c* and 3*d* sites, respectively; during the transition, the Nb atoms migrate within the *a* + *c* sublattice, as well as O atoms migrate within the *b* + *d* sublattice. After the transformation, the occupancies of the Nb sublattice (*a* and *c* in *Pm*-3 *m*) and the O sublattice (*b* and *d* in *Pm*-3 *m*) become equivalent and equal to 75%. Therefore, the SG transforms to *Fm*-3 *m*, and the Wyckoff sites for Nb and O in the transformed structure are 4*a* and 4*b* in *Fm*-3 *m*. The unit cell axes *a*, *b* and *c* are marked by red, green and blue arrows.

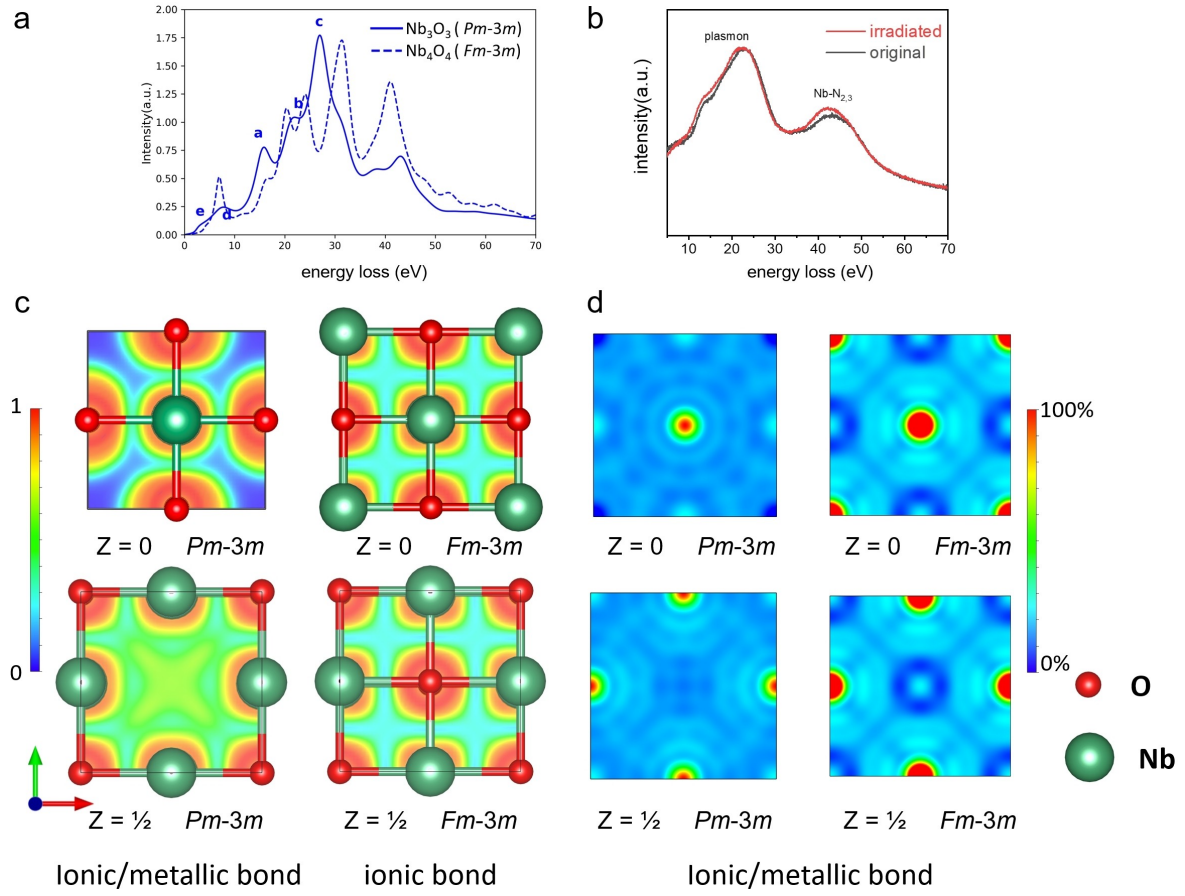

Figure 5. (a) Comparison of the theoretical EELF result obtained with the structure model of the pristine structure (Nb_3O_3, *Pm*-3 *m*) and the hypothetical rock salt structure (Nb_4O_4, *Fm*-3 *m*). (b) EELS data collected from the same area before and after electron beam irradiation. (c) Comparison of the ELF results obtained with the pristine structure (Nb_3O_3, *Pm*-3 *m*) and the hypothetical rock salt structure (Nb_4O_4, *Fm*-3 *m*). (d) Electrostatic potential map of Nb_3O_3 before structural transformation in *Pm*-3 *m* and after structural transformation in *Fm*-3 *m* reconstructed from the 3D ED data. Z = 0 and 1/2 correspond to the Nb-O_4 and Nb_4-O_4 planes in the *Pm*-3 *m* SG (see Figure 5c). In *Fm*-3 *m*, the two planes are geometrically identical. Unit cell axes *a*, *b* and *c* are marked by red, green and blue arrows, respectively.

characteristic edges in the EELF were expected to match with the experimental EELS data. The major difference between *Pm*-3 *m* Nb_3O_3 structure and the hypothetical rock salt structure in the EELF are the edges at 30 eV and 40 eV. Figure 5b shows the EELS experimental data for the Nb-$N_{2,3}$ edges collected from the original and the irradiated sample; however, the major difference at 30 eV and 40 eV was not observed, being both of them similar to the EELF of the pristine Nb_3O_3. Additional EELS data are depicted in Figure S18, showing no significant differences between the original and the transformed material, which indicates that the structure after transformation may not be the ideal rock salt structure with 100% occupancy but it would maintain a similar electronic state as Nb_3O_3.

To analyze this aspect, the Electron Localization Function (ELF) was calculated for *Pm*-3 *m* Nb_3O_3 and the hypothetical rock salt Nb_4O_4, see Figure 5c. The results show a coexistence of ionic and metallic bonds in the *Pm*-3 *m* (Nb_3O_3) with significant residual electron localization between atoms. While for the rock salt structure, only ionic bonds dominate. The ionic-metallic properties could also be revealed by the physical characteristics of Nb_3O_3. Figure S19 shows optical micrographs of Nb_3O_3 revealing both metallic-shine and cleavage surfaces. By STEM-HAADF imaging, together with SAED and FFT diffractograms, the cleavage surface index preference could be recognized as {100} and {110}, see Figure S20.

From the electron density map of the pristine Nb_3O_3 reconstructed from the SCXRD and the electric potential map reconstructed from 3D ED, the metallic-ionic property was also evidenced. In Figure S7 the electron density map reconstructed from SCXRD of the pristine Nb_3O_3, it could be observed that there was a residual electron distribution between atoms, which was in agreement with the unlocalized metallic bond distribution observed in the ELF results. In the 3D ED electrostatic potential map reconstruction, collected from the same NbO crystal before and after structural transformation, the pure ionic property was not observed in the transformed structure (Figure 5d). In the electrostatic potential map of the *Pm*-3 *m* structure, a residual electrostatic potential (similar to the ELF and SCXRD results), could be observed. For the 3D ED electrostatic potential map after transformation, even for *Fm*-3 *m* SG, the residual electrostatic potential could still be observed, which was similar to the electron distribution of Nb_3O_3 *Pm*-3 *m*.

Research Article
doi.org/10.1002/chem.202300614
Chemistry Europe
European Chemical Societies Publishing

This indicates that the unlocalized metallic electron distribution remains after transformation.

Based on the maintenance of the unlocalized electron distribution, it could be inferred that in the transformed Nb_3O_3, *Fm*-3 *m*, the ionic-metallic bonds coexistence remained, which means that the 4-coordinated bonding was maintained, and the manner in which the structure was transformed consisted in the translation of atoms. A two-unit cell structural model was built to simulate the structural transformation, in which the second unit cell (on the top) was shifted (original Nb (*c*) site towards the vacant Nb (*a*) site) with the assumption that electron beam radiation does not change the electron composition, but only laterally shifts the top layer of the sample. We calculated and compared the total energy with respect to the original one to see if such a lateral shift was energetically plausible, see Figure 6. Figure 6a shows the original two-unit cell model (pristine material) along the *a*-axis, with a slight tilting for better visualization (top) and along the *c*-axis (bottom). The final structure after the shift is shown in Figure 6c, where the yellow arrow tracks the lateral shift of the top layer. The relative total energy with respect to the pristine material is shown in Figure 6b; under the continuous shift, the total energy difference increased, reaching a maximum when the unit cell was displayed by one quarter.

After that, the relative energy began to decrease and finally reached a lower value than that of the initial state (pristine material), suggesting that it was energetically preferable for the Nb atom to partially migrate from the *c* site to the *a* site. Therefore, the electron beam would act as a stimulus providing the driving force to trigger the lateral shift.

The migration of atoms (one Nb in 3*c* exchange with Nb vacancy in 1*a*, one O in 3*d* exchange with O vacancy in 1*b*), would generate an antiphase defect, which was actually observed in the pristine Nb_3O_3 material. Figure 7 shows the models proposed and the C_s-corrected STEM-HAADF analysis of the antiphase planar defects along [100] and [111] directions. The planar defects could be described as a {110} glide plane, with the two domains gliding parallel along the {110} plane with a distance of half a diagonal unit cell. In the boundary of

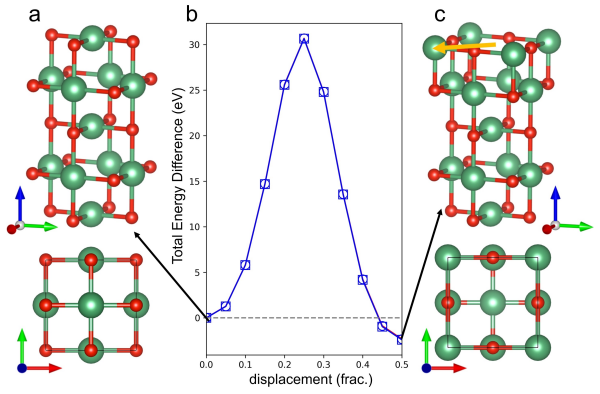

Figure 6. Total energy difference vs. Nb displacement based on a two-unit cell model. (a) Two-unit cell model corresponding to the pristine Nb_3O_3 structure from side and top view. (b) Energy difference calculation with respect to Nb atom displacement. (c) Transformed two-unit cell model with a 0.5 unit cell Nb atom displacement. The path of the Nb atom shift is marked by the yellow arrow, the unit cell axes *a*, *b* and *c* are in red, green and blue arrows respectively.

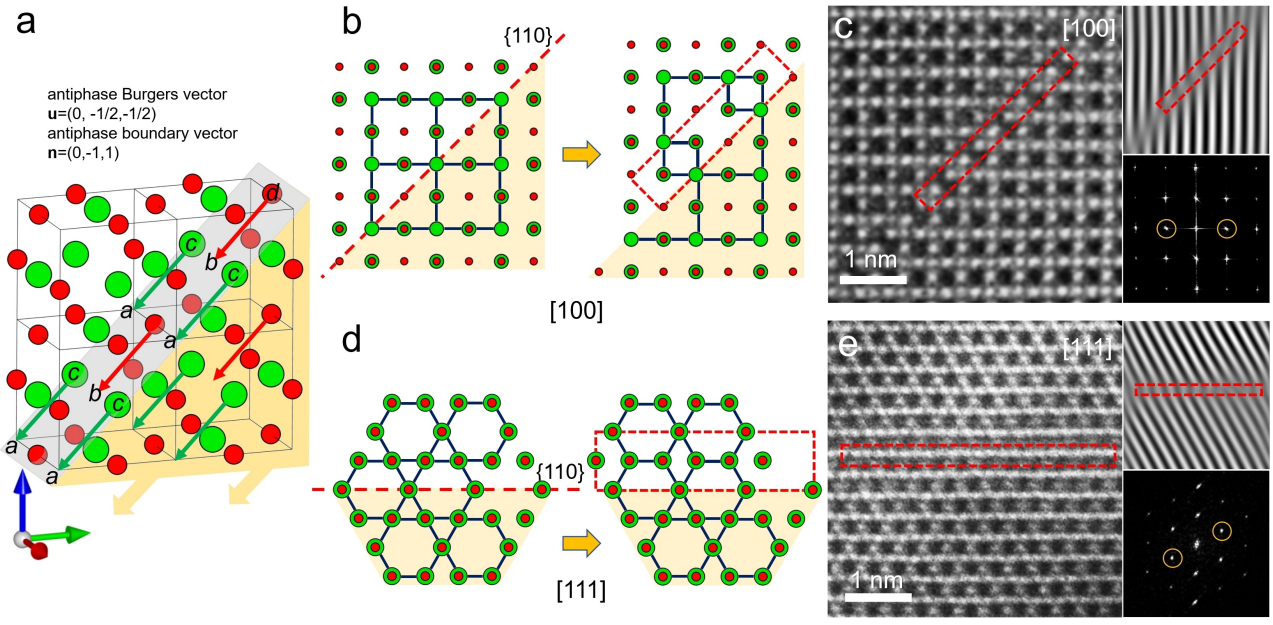

Figure 7. Illustration and STEM-HAADF images showing antiphase planar defects in pristine NbO. (a) Illustration of the atoms dislocation in the antiphase structure. The atoms dislocation are marked by arrows and the antiphase boundary is marked in grey. The unit cell axes *a*, *b* and *c* are marked by red, green and blue arrows. (b,d) Structure model of NbO antiphase glide along the {110} plane, viewed along [100] and [111]. Two sides of domain are marked in different colours, the antiphase boundary is marked by the red dashed line, and unit cells are marked in blue. (c,e) STEM-HAADF images of antiphase planar defect along [100] and [111] with FFT diffractogram and spot mask filtered image inset. The antiphase boundary is marked by the red dashed line, masked spots are marked by yellow circles.

the two sides, the dislocation of atoms was exactly the Nb atom shifts from the *c* site to the *a* site and O atom shifts from the *d* site to the *b* site. This planar defect evidenced the existence of an antiphase structure. In an antiphase structure, the translational symmetry of two domains, sharing the same ordered structure, will be broken at the antiphase boundary (APB).[18] In Figure 7a, the antiphase Burger vector (marked by arrows), from *c* to *a* or *d* to *b*, is indexed as $\mathbf{u}=(0, -1/2, -1/2)$, and the APB plane vector is indexed by $\mathbf{n}=(0, -1, 1)$. The relationship between them agrees with the rule of a conservative APB, $\mathbf{u}\cdot\mathbf{n}=0$, suggesting that no chemical composition change would be expected[19] as it has been experimentally observed. Figures 7b and 7d show the structural model of the antiphase planar defect observed along the [100] and [111] directions. The regions marked in light yellow are the domains that were translated along the diagonal (red dashed line) by half of the unit cell, while the APB is marked with a red dashed line. The C_s-corrected STEM-HAADF images of the antiphase structure along [100] and [111] are depicted in Figures 7c and e, with the APB marked by a dashed red line. To clearly observe the antiphase structure, the image was mask filtered using two reflections that contained information of the phase dislocation (yellow circles in the FFT diffractogram). In the filtered image top right, a distinct phase change was observed at the antiphase boundary marked in red. During EM observation, such defects were rarely observed, and most of the NbO crystals were single crystals. However, a low magnification image of a region of pristine NbO "rich" with defects is presented in figure S21.

To simulate the {110} antiphase boundary, we further constructed a lateral shift interface model of two pristine Nb_3O_3 blocks, see Figure S22, and calculated the relative energy change during the shift. In the interface plane, both Nb and O atoms shift by 1/2(***a***-***c***) along the [101] direction. The total energy difference per atom and the energy barrier were both reasonably small with a high probably for the lateral shift to occur under the electron beam radiation.

This APB could then be considered as the first step observed in the transformation mechanism induced by the electron beam, in which some Nb and O atoms occupy the original vacant positions. In the Nb_3O_3 structure, one atom is surrounded by four nearest fcc sublattice vacancy positions, and the Nb(*c*) and O(*d*) atoms would randomly migrate to the nearest *a* and *b* positions, respectively, forming a local antiphase domain, and increasing the occupancy at the *a* and *b* sites. When the process is completed, averaged equivalent 75% occupancy probabilities for Nb at 1*a* and 3*c*, and for O at 1*b* and 3*d*, are observed. Within each antiphase domain, the chemical environment (including the electron valance state and the chemical composition) is not expected to be changed, as observed in the transformed Nb_3O_3 structure by 3D ED, EELS analysis and DFT calculations.

Conclusion

In this work, we have presented an exhaustive analysis of Nb_3O_3 starting from the pristine material and following the structural transformation that takes place under electron beam irradiation. The pristine Nb_3O_3 structure was unambiguously solved by combining the information obtained from PXRD, SCXRD, density measurement and elemental chemical analysis resulting in a unit cell containing 3 atoms of Nb and 3 atoms of O with the *Pm*-3 *m* space group, where Nb and O are located at 3*c* (0, 1/2, 1/2), (1/2, 0, 1/2), (1/2, 1/2, 0) and 3*d* (1/2, 0, 0), (0, 1/2, 0), (0, 0, 1/2) sites, respectively. The sites at 1*a* (0, 0, 0) and 1*b* (1/2, 1/2, 1/2) are not occupied by any atom in the pristine material. The structural transformation was then followed by atomic resolution electron microscopy, observing that Nb migrates to the 1*a* sites while O migrates to the 1*b* sites until the occupancies are equivalent. In the final transformed structure, the space group is *Fm*-3 *m* with all four possible sites (1*a* and 3*c* for Nb; 1*b* and 3*d* for O) occupied with 75% occupancy, but maintaining the Nb_3O_3 chemical composition, as confirmed by theoretical DFT calculations and spectroscopic analysis.

Antiphase boundaries are observed in the pristine material generating a structure very similar to the first steps of the structural transformation initiated by electron beam irradiation.

Experimental Section

Synthesis of NbO: In the 1960's, the structures of TMO (TM–Ti, V and Nb) with TM/O ratio close to 1 attracted a lot of interest due to the existence of vacancies and their arrangements to explain their physical properties. At that time, one of the authors (OT) studied the structures of Ti–O and V–O by PXRD and EM, and prepared a NbO single crystal at Tohoku University for the next study. The synthesis process was following: first, an NbO rod was prepared by melting a proper mixture of Nb metal-sponge and Nb_2O_5 powder with arc-melt, shaping it into a cylindrical rod, then the NbO single crystal was grown from the rod by floating-zone method with high-frequency furnace. The crystals show shiny gold colour and clear cleavage, which are typical features of metallic and ionic crystals, respectively.

Density measurement: The Density of NbO crystals was measured based on Archimedes principle on a density analytical balance. The Weight of NbO was first measured in dry air, then a NbO crystal was suspended and immersed in purified water to measure the buoyancy. The density of sample was calculated based on the known density of water and air at 20 °C.

X-ray diffraction analysis: PXRD measurement was performed in a Rigaku *SmartLab* automated multipurpose X-ray diffractometer equipped with a monochromator for Cu $K\alpha_1$ primary unit incidence. The NbO sample was crushed from the large single crystal into a powder state and loaded in a glass capillary tube. The capillary tube has an outside diameter of 0.2 mm and a wall thickness of 0.01 mm. PXRD data was collected using the Debye Scherrer method in transmission step-scan mode with 0.1°/min scan speed from 10° to 115° with 0.01° step size.

Using Mo Kα radiation, SCXRD data were collected from a piece of NbO with a diameter about 100 μm in a PHOTON III detector (Bruker D8 Venture). Diffraction data was reduced by *CrysAlisPro* software. The empirical absorption correction used spherical

harmonics, implemented in the SCALE3 ABSPACK scaling algorithm. Using *Olex2*,[20] the structure was solved with the *SHELXT*[21] structure solution program using *Intrinsic Phasing* and refined with the *SHELXL*[22] refinement package using *Least Squares* minimization.

C_s-corrected STEM and SAED observation: NbO was deeply crushed into a fine powder using mortar and pestle. It was then dispersed in HPLC ethanol under ultrasonic treatment for 5 min. Afterwards, the solution was dropped onto a TEM copper grid with ultrathin carbon film and dried under infrared light.

Atomic resolution STEM-HAADF images were taken in a C_s-corrected STEM, JEM-ARM300F, with cold FEG and a double tilt holder operated at 300 kV. STEM images were recorded using a 30 μm condenser lens aperture forming an electron probe convergence semiangle of 24 mrad, the STEM probe current was measured as 30.7 pA. The collection angle for the HAADF data was 54–220 mrad. Aberration correction was executed by *COSMO* software, which is connected to the instrument and collects Ronchigram of the electron probe at amorphous carbon.[23] SAED patterns were collected from the area of interest using SA aperture in diffraction mode. Both TEM images and SAED patterns were recorded on a TEM JEM-2100Plus, with LaB_6 and TVIPS camera operated at 200 kV.

3D ED analysis: 3D ED data from the original and from the irradiated NbO crystals were collected on a JEM-ARM300F Grand ARM using a double tilt holder. The electron diffraction series were collected by recording an in-situ video using Gatan OneView camera with continuous goniometer tilting. The goniometer tilting speed was measured as 1.8°/s, and the frame exposure time was set to 0.3 s resulting in a 0.45° frame angle increment. For pristine NbO, 126 electron diffraction pattern frames were collected, covering a 67.5° angle range. Then, this single crystal was irradiated in STEM mode during 30 mins, using a probe current of 204 pA to ensure that the structure was fully transformed. After irradiation, another 3D ED dataset was collected under the same conditions as for the pristine one. 117 electron diffraction frames covering 62.64° were collected. The collected 3D ED data were loaded in PETS2 to extract diffraction intensities, and the structure were solved and refined by JANA 2020.

EDS elemental analysis: Energy Dispersive X-ray Spectroscopy (EDS) elemental mapping and chemical analysis were performed in a JEOL F200 TEM equipped with a Schottky type-emission gun and JEOL EDS detector operated at 200 kV. The averaged chemical composition was obtained after analyzing 20 different crystals.

EELS analysis: EELS data before and after irradiation were collected on a Grand JEM-ARM300F at 300 kV in STEM mode by Gatan 965 GIF Quantum ER spectrometer. Low energy spectra including zero loss peak, plasmon and Nb-$N_{2,3}$ edges were collected on a US1000FTXP camera, middle and high energy spectra including Nb-$M_{4,5}$, Nb-$M_{2,3}$, Nb-$L_{2,3}$, and O–K edges were collected on a retractable direct detection Gatan camera (K2). Alignment of filter was individually adjusted for each camera when collecting corresponding spectra or spectral images. To maintain the pristine structure as much as possible, a low dose was employed to analyze the original material. No signs of structural transformation were observed after the measurement.

Elemental analysis was performed on the middle range energy spectra based on the Nb-$M_{4,5}$ and O–K edges. Spectra were collected from two regions of the pristine material and of the transformed material in 2D scan mode. The elemental composition of the two regions were determined by Nb-$M_{4,5}$ and O–K characteristic edges in the integrated spectra of the full collected regions.

SEM observation: Scanning EM (SEM) images were taken using a JEOL JSM-7800F Prime instrument. Crushed NbO powder was dropped onto conductive tape, which was stuck on a copper SEM sample stage and blown by compressed air to remove residual sample. For imaging, GB (gentle beam) mode was employed; in this mode, a 2 kV bias voltage was generated on the sample stage, and the electron probe could gently land on the sample avoiding charging effects while maintaining very good spatial resolution using a high accelerating voltage. The accelerating voltage of the electron probe was 3 kV, and the landing voltage after bias was 1 kV.

Ab initio Calculations: We performed the density functional theory study of NbO with the *Quantum Espresso* package.[24] The calculations were done with the generalized gradient approximation and the projector augmented wave pseudopotential as obtained in *PS library*[25] for the electronic properties and geometric optimization. The input file was generated with *"Materials Cloud" Quantum Espresso input generator*.[26] The Brillouin zone discretization was $8\times8\times8$ for the bulk and $8\times8\times2$ for the interface/surface obtained within the *Monkhorst–Pack* scheme.[27] The kinetic energy cutoff was chosen as 50 Ry for wave functions and 400 Ry for charge density and potentials. During relaxation, the convergence threshold was 8×10^{-5} eV on total energy and 1×10^{-4} eV/Å on forces.

Acknowledgements

The authors would like to thank to the Centre for High-resolution Electron Microscopy (*ChEM*, EM02161943) and Shanghai Key-Laboratory of HREM (21DZ2260400), ShanghaiTech University. AM acknowledges the Spanish Ministry of Science (RYC2018-024561-I) the regional government of Aragon (DGA E13_20R) the National Natural Science Foundation of China (NSFC-21835002). GL acknowledges the National Key R&D Program of China (2022YFA1402703), National Natural Science Foundation of China (11874263), Shanghai 2021-Fundamental Research Aera (21JC1404700), Shanghai Technology Innovation Action Plan (20DZ1100605), and Sino-German Mobility program (M-0006). Calculations were performed at the HPC Platform of ShanghaiTech University Library and Information Services, and at the School of Physical Science and Technology. Prof. Jihong Yu is acknowledged for encouragement to JL, who is working at ShanghaiTech University as an exchange PhD student. Prof. Kenneth Harris is acknowledged for scientific discussions.

Conflict of Interests

The authors declare no conflict of interest.

Data Availability Statement

The data that support the findings of this study are available from the corresponding author upon reasonable request.

Keywords: C_s-corrected STEM · 3D ED · DFT calculation · NbO · structure transformation

[1] a) O. Kubaschewski, B. Hopkins, *J. Less-Common Met.* **1960**, *2*, 172–180; b) J. A. Roberson, R. A. Rapp, *J. Phys. Chem. Solids* **1969**, *30*, 1119–1124; c) Y. Tokura, N. Nagaosa, *Science* **2000**, *288*, 462–468; d) M. Backhaus-Ricoult, J. Rustad, L. Moore, C. Smith, J. Brown, *Appl. Phys. A* **2014**, *116*, 433–470; e) J. B. Goodenough, *Chem. Mater.* **2014**, *26*, 820–829.
[2] a) D. K. Finnemore, T. F. Stromberg, C. A. Swenson, *Phys. Rev.* **1966**, *149*, 231–243; b) I. Nowak, M. Ziolek, *Chem. Rev.* **1999**, *99*, 3603–3624; c) A. J. Deardo, *Int. Mater. Rev.* **2003**, *48*, 371–402; d) D. R. Lide, *handbook of chemistry and physics, Vol. 85*, CRC press, **2004**.
[3] a) C. Nico, T. Monteiro, M. P. F. Graça, *Prog. Mater. Sci.* **2016**, *80*, 1–37; b) A. I. Gusev, *JETP Lett.* **2020**, *111*, 176–182.
[4] a) G. Andersson, *Acta Chem. Scand.* **1954**, *8*, 1599–1606; b) C. Piccirillo, R. Binions, I. P. Parkin, *Chem. Vap. Deposition* **2007**, *13*, 145–151; c) T. K. Le, P. V. Pham, C.-L. Dong, N. Bahlawane, D. Vernardou, I. Mjejri, A. Rougier, S. W. Kim, *J. Mater. Chem. C* **2022**, *10*, 4019–4071.
[5] B. Predel, in *Landolt-Börnstein – Group IV Physical Chemistry, Vol. 5I: "Ni-Np – Pt-Zr"*, Springer-Verlag Berlin Heidelberg.
[6] a) R. E. Loehman, C. N. R. Rao, J. M. Honig, *J. Phys. Chem.* **1969**, *73*, 1781–1784; b) P. S. Bell, M. H. Lewis, *Phys. Status Solidi A* **1971**, *7*, 431–439; c) B. Andersson, J. Gjønnes, A. R. Forouhi, *J. Less-Common Met.* **1978**, *61*, 273–291; d) J. K. Burdett, T. Hughbanks, *J. Am. Chem. Soc.* **1984**, *106*, 3101–3113; e) S. Ikeda, N. Sugiyama, S.-y. Murakami, H. Kominami, Y. Kera, H. Noguchi, K. Uosaki, T. Torimoto, B. Ohtani, *Phys. Chem. Chem. Phys.* **2003**, *5*, 778–783; f) A. I. Gusev, D. A. Davydov, A. A. Valeeva, *J. Alloys Compd.* **2011**, *509*, 1364–1372; g) Z. Su, J. Liu, M. Li, Y. Zhu, S. Qian, M. Weng, J. Zheng, Y. Zhong, F. Pan, S. Zhang, *Electrochem. Energy Rev.* **2020**, *3*, 286–343.
[7] a) B. Predel, in *Landolt-Börnstein – Group IV Physical Chemistry, Vol. 5H: "Li-Mg – Nd-Zr"*, Springer-Verlag Berlin Heidelberg; b) J. Hulm, C. Jones, R. Hein, J. Gibson, *J. Low Temp. Phys.* **1972**, *7*, 291–307; c) C. Nico, M. Soares, J. Rodrigues, M. Matos, R. Monteiro, M. Graça, M. Valente, F. Costa, T. Monteiro, *J. Phys. Chem. C* **2011**, *115*, 4879–4886; d) C. Nico, L. Rino, M. Matos, R. Monteiro, F. M. Costa, T. Monteiro, M. P. Graça, *J. Eur. Ceram. Soc.* **2013**, *33*, 3077–3083.
[8] a) O. M. Yaghi, M. O'Keeffe, N. W. Ockwig, H. K. Chae, M. Eddaoudi, J. Kim, *Nature* **2003**, *423*, 705–714; b) A. Galet, V. Niel, M. C. Muñoz, J. A. Real, *J. Am. Chem. Soc.* **2003**, *125*, 14224–14225; c) B. Chen, N. W. Ockwig, F. R. Fronczek, D. S. Contreras, O. M. Yaghi, *Inorg. Chem.* **2005**, *44*, 181–183; d) M. O'Keeffe, M. A. Peskov, S. J. Ramsden, O. M. Yaghi, *Acc. Chem. Res.* **2008**, *41*, 1782–1789; e) M. L. Cao, H. G. Hao, W. X. Zhang, B. H. Ye, *Inorg. Chem.* **2008**, *47*, 8126–8133; f) G. G. Hou, Y. Liu, Q. K. Liu, J. P. Ma, Y. B. Dong, *Chem. Commun.* **2011**, *47*, 10731–10733; g) M. O'Keeffe, O. M. Yaghi, *Chem. Rev.* **2012**, *112*, 675–702; h) X. Wang, M. Bahri, Z. Fu, M. A. Little, L. Liu, H. Niu, N. D. Browning, S. Y. Chong, L. Chen, J. W. Ward, A. I. Cooper, *J. Am. Chem. Soc.* **2021**, *143*, 15011–15016.
[9] a) A. L. Bowman, T. C. Wallace, J. L. Yarnell, R. G. Wenzel, *Acta Crystallogr.* **1966**, *21*, 843; b) E. Wimmer, K. Schwarz, R. Podloucky, P. Herzig, A. Neckel, *J. Phys. Chem. Solids* **1982**, *43*, 439–447; c) E. Z. Kurmaev, A. Moewes, O. G. Bureev, I. A. Nekrasov, V. M. Cherkashenko, M. A. Korotin, D. L. Ederer, *J. Alloys Compd.* **2002**, *347*, 213–218; d) W. W. Schulz, R. M. Wentzcovitch, *Phys. Rev. B* **1993**, *48*, 16986–16991.
[10] a) G. Brauer, *Naturwissenschaften* **1940**, *28*, 30–30; b) G. Andersson, A. Magneli, *Vol. 11*, Munksgaard Int Publ Ltd., **1957**, pp. 1065–1066; c) R. W. G. Wyckoff, *Crystal structures, Vol. 1*, Interscience Publishers, New York, **1963**.
[11] T. Onozuka, M. Koiwa, Y. Ishikawa, S. Yamaguchi, M. Hirabayashi, *Radiat. EIT.* **1977**, *31*, 117–123.
[12] A. Mayoral, Y. Ma, O. Terasaki, *Isr. J. Chem.* **2018**, *58*, 1157–1163.
[13] a) O. Krivanek, N. Dellby, A. Spence, L. Brown, *Electron Microsc.* **1988**; b) C. Li, Q. Zhang, A. Mayoral, *ChemCatChem* **2020**, *12*, 1248–1269.
[14] a) M. Gemmi, E. Mugnaioli, T. E. Gorelik, U. Kolb, L. Palatinus, P. Boullay, S. Hovmöller, J. P. Abrahams, *ACS Cent. Sci.* **2019**, *5*, 1315–1329; b) P. Ercius, O. Alaidi, M. J. Rames, G. Ren, *Adv. Mater.* **2015**, *27*, 5638–5663.
[15] Ehrhart, in *Landolt-Börnstein, Vol. 25*, New Series III ed., Springer, **1991**, p. 88.
[16] A. Mayoral, T. Carey, P. A. Anderson, A. Lubk, I. Diaz, *Angew. Chem. Int. Ed.* **2011**, *50*, 11230–11233; *Angew. Chem.* **2011**, *123*, 11426–11429.
[17] a) V. Petříček, M. Dušek, L. Palatinus, *Zeitschrift für Kristallographie-Crystalline Materials* **2014**, *229*, 345–352; b) L. Palatinus, P. Brázda, M. Jelínek, J. Hrdá, G. Steciuk, M. Klementová, *Acta Crystallogr. Sect. B* **2019**, *75*, 512–522.
[18] a) R. Kikuchi, J. W. Cahn, *Acta Metall.* **1979**, *27*, 1337–1353; b) J. M. Howe, *14 - Structure, Composition and Energy of Solid–Solid Interfaces*, Elsevier, Oxford, **2014**.
[19] P. A. Flinn, *Trans. Am. Inst. Min. Metall. Eng.* **1960**, *218*, 145–154.
[20] O. V. Dolomanov, L. J. Bourhis, R. J. Gildea, J. A. Howard, H. Puschmann, *J. Appl. Crystallogr.* **2009**, *42*, 339–341.
[21] G. M. Sheldrick, *Acta Crystallogr. Sect. A* **2015**, *71*, 3–8.
[22] G. M. Sheldrick, *Acta Crystallogr. Sect. C* **2015**, *71*, 3–8.
[23] A. R. Lupini, P. Wang, P. D. Nellist, A. I. Kirkland, S. J. Pennycook, *Ultramicroscopy* **2010**, *110*, 891–898.
[24] P. Giannozzi, S. Baroni, N. Bonini, M. Calandra, R. Car, C. Cavazzoni, D. Ceresoli, G. L. Chiarotti, M. Cococcioni, I. Dabo, A. Dal Corso, S. de Gironcoli, S. Fabris, G. Fratesi, R. Gebauer, U. Gerstmann, C. Gougoussis, A. Kokalj, M. Lazzeri, L. Martin-Samos, N. Marzari, F. Mauri, R. Mazzarello, S. Paolini, A. Pasquarello, L. Paulatto, C. Sbraccia, S. Scandolo, G. Sclauzero, A. P. Seitsonen, A. Smogunov, P. Umari, R. M. Wentzcovitch, *J. Phys. Condens. Matter* **2009**, *21*, 395502.
[25] A. Dal Corso, *Comput. Mater. Sci.* **2014**, *95*, 337–350.
[26] "Quantum ESPRESSO input generator and structure visualizer" can be found under http://www.materialscloud.org/work/tools/qeinputgenerator.
[27] H. J. Monkhorst, J. D. Pack, *Phys. Rev. B* **1976**, *13*, 5188–5192.

Manuscript received: February 24, 2023
Accepted manuscript online: April 3, 2023
Version of record online: April 27, 2023